JATIS Journal of Astronomical Telescopes, Instruments, and Systems

RESEARCH PAPER

Rapid characterization of exoplanet atmospheres with the Exoplanet Transmission Spectroscopy Imager

Luke M. Schmidt,[a,b,c,d,*] Ryan J. Oelkers,[a,b,c,e] Erika Cook,[a,b,c] Mary Anne Limbach,[f] Darren L. DePoy,[a,b,c] Jennifer L. Marshall,[a,b,c] Landon Holcomb,[a,c] Willians Pena,[a,c] Jacob Purcell,[a,c,g] and Enrique Gonzalez Vega[a,c]

[a]Texas A&M University, Department of Physics and Astronomy, College Station, Texas, United States
[b]Texas A&M University, George P. and Cynthia Woods Mitchell Institute for Fundamental Physics and Astronomy, College Station, Texas, United States
[c]Texas A&M University, Department of Physics and Astronomy, Charles R. and Judith G. Munnerlyn Astronomical Laboratory, College Station, Texas, United States
[d]Yerkes Observatory, Williams Bay, Wisconsin, United States
[e]The University of Texas, Rio Grande Valley, Department of Physics and Astronomy, Brownsville, Texas, United States
[f]University of Michigan, Department of Astronomy, Ann Arbor, Michigan, United States
[g]Indiana University—Purdue University at Indianapolis, Department of Physics, Indianapolis, Indiana, United States

ABSTRACT. The Exoplanet Transmission Spectroscopy Imager (ETSI) amalgamates a low-resolution slitless prism spectrometer with custom multi-band filters to simultaneously image 15 spectral bandpasses between 430 and 975 nm with an average spectral resolution of $R = \lambda/\delta\lambda \sim 20$. ETSI requires only moderate telescope apertures (~2 m), is capable of characterizing an exoplanet atmosphere in as little as a single transit, enabling the selection of the most interesting targets for further characterization with other ground and space-based observatories, and is also well suited to multi-band observations of other variable and transient objects. This enables a new technique, common-path multi-band imaging, used to observe transmission spectra of exoplanets transiting bright ($V < 14$ magnitude) stars. ETSI is capable of near photon-limited observations, with a systematic noise floor on par with the Hubble Space Telescope and below the Earth's atmospheric amplitude scintillation noise limit. We report the as-built instrument optical and optomechanical design, detectors, control system, telescope hardware and software interfaces, and data reduction pipeline. A summary of ETSI's science capabilities and the initial results are also included.

Keywords: exoplanets; transmission spectroscopy; multi-band filters; precision photometry; transits

Paper 24107G received Jul. 12, 2024; revised Oct. 25, 2024; accepted Nov. 21, 2024; published Dec. 9, 2024.

1 Introduction

The advantages of simultaneous multi-band photometry were leveraged by astronomers in the mid-20th century. Early experiments with photomultiplier tubes by Walraven and Walraven[1]

*Address all correspondence to Luke M. Schmidt, lschmidt@yerkesobservatory.org

resulted in the Walraven five-channel spectrophotometer along with other instruments such as the Danish $uvby-\beta$ five-channel spectrophotometer.[2] These instruments demonstrated that simultaneous measurement of multiple bands is superior to sequential observations of multiple bands when measuring relative colors of astronomical objects. Examples of simultaneous multi-band photometry observations include stellar pulsations of subluminous B (sdB) stars,[3] constraining physical properties of transiting exoplanets,[4] changes in the spectral energy distribution of supernovae,[5] and characterization of spots on M-dwarf stars.[6] Changes in seeing and transparency can still affect the recorded brightness of an object, but any variable absorption (e.g., clouds), which is colorless, has the same effect on all wavelengths,[7,8] leaving relative color measurements unaffected if the measurements are made simultaneously. The first multi-band instruments were complex and required very stable environments as the bandpass selection was performed by slicing a dispersed spectrum with a set of prisms. Any flexure or motion of the star in the instrument's field of view could change the bandpass seen in a given channel. Other multi-band instruments involved multiple telescopes observing with different filters[9] or multiple dichroics, filters, and detectors, one for each bandpass,[10–16] which become unwieldy beyond only a few bandpasses due to mechanical space constraints as well as transmission losses for channels at the end of the chain of stacked dichroics. Fortunately, recent advances in thin film coating technology[17] have enabled the creation of filters with many bandpasses selected by a single optic and when used in both transmission and reflection enable simultaneous measurement of many more bandpasses with only two detectors.

In this paper, we describe the instrument design, construction, and commissioning activities as well as a brief description of the wide variety of objects and types of observations that are well matched to the Exoplanet Transmission Spectroscopy Imager (ETSI)'s capabilities. We also highlight the benefits of using ETSI as a reconnaissance instrument to optimize observations with the James Webb Space Telescope[18] (JWST), or as a rapid follow-up instrument for transient alerts from the Vera C. Rubin Observatory Legacy Survey of Space and Time (LSST).[19]

2 ETSI Instrument

The ETSI[20,21] is based on traditional slitless spectroscopy, with a novel multi-band filter used to split a continuous spectrum into multiple distinct spectral bands, enabling traditional point spread function (PSF) fitting or aperture photometry of each band. This is more efficient and uncomplicated compared with other exoplanet transmission spectroscopy data reduction pipelines (examples in Refs. 22 and 23). The complexities of these pipelines, which can include binning higher-resolution spectra, wavelength calibration, and spectral fitting techniques, may introduce biases to the retrieved information.[24] The common optical path and the simultaneous nature of ETSI observations mean that any instrumental or environmental common path errors, including atmospheric scintillation, are greatly reduced. By referencing one science target spectral band to another science target band, color changes on the order of 0.006% over the course of transit are detectable (see Sec. 6). The ETSI optical design was optimized to ensure that the point source 80% encircled energy at all wavelengths is well below typical seeing (1 to 2 arcseconds) and that the PSF's would not appreciably change shape for small changes in focus (see Fig. 1 for wavelength dependent spot diagram and Table 1 for as built performance). This minimizes residual color errors due to wavelength-dependent PSF changes during an observation.

ETSI does not measure absolute transit depth in each spectral band, instead it measures relative transit depth between each band. Once an image sequence is obtained on-sky using this instrument, we use a self-referencing differential photometric technique to eliminate sources of uncertainty from non-common path sources such as atmospheric scintillation, instrumental effects, and telescopic effects. To do this, we ratio each spectral band of the science star to another spectral band of the same science star [see Eq. (1) below], which differs from traditional photometric measurements made by rationing the flux of the science target to one or more reference stars [see Eq. (2) below]

$$f(\text{target})_i = f(\text{target})_i'/f(\text{target})_j', \tag{1}$$

where $f(\text{target})_i$ is the detrended flux for the i'th bandpass, $f(\text{target})_i'$ is the raw flux from the i'th bandpass, and $f(\text{target})_j'$ is the raw flux from the reference bandpass, j

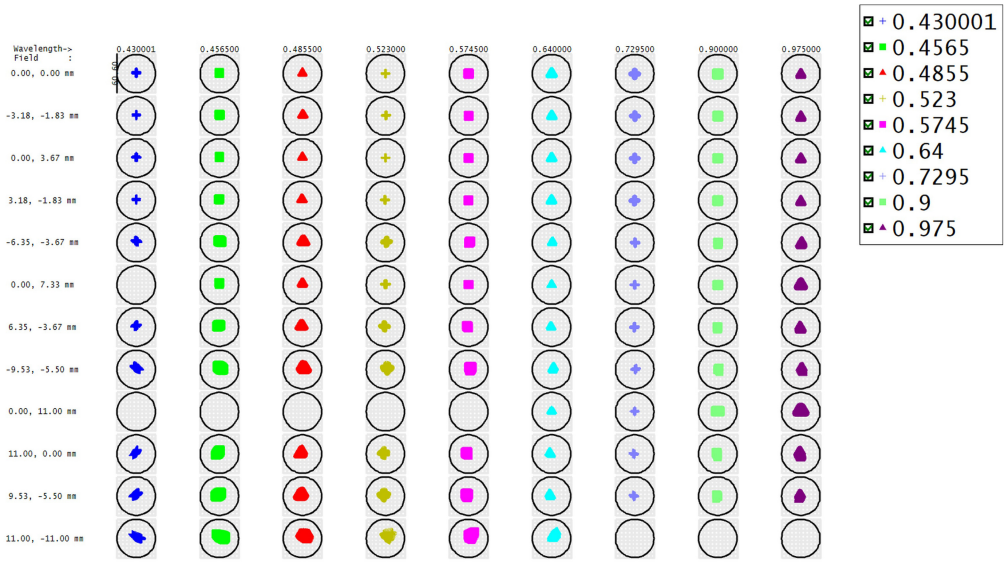

Fig. 1 Matrix spot diagram of ETSI and a paraxial McDonald Observatory 2.1-m telescope. The circles are 1 arcsecond in diameter. The field positions with missing spots are at the edge of the field and those wavelengths fall off the edge of the detector (2048×2048, 11-μm pixels).

Table 1 Collimator and cameras as-built optical performance. Requirement was on-axis 80% encircled energy within a 25.4-μm spot size for the collimator and on-axis 80% encircled energy within a 12.7-μm spot size for the cameras, tested at three wavelengths. The cameras and collimator were tested separately, rather than in combination, as it did not require the vendor to develop a custom test bench.

Filter (nm)	Field position	Collimator EE80 (μm)	Camera 1 EE80 (μm)	Camera 2 EE80 (μm)
440	On axis	5.2	7.6	4.2
632	On axis	11.5	5.1	9.4
900	On axis	7.6	6.0	7.9

$$f(\text{target})_i = f(\text{target})_i'/f(\text{comp})_i, \tag{2}$$

where $f(\text{target})_i$ is the detrended flux for the target star in the i'th bandpass, $f(\text{target})_i'$ is the raw flux from the target star in the i'th bandpass, and $f(\text{comp})_i$ is the raw flux from the comparison star in the i'th bandpass. Our initial on-sky results show that the highest precision measurements are obtained by using a spectral band near the middle of the ETSI spectral range as our reference band. ETSI color precision is typically limited by photon noise from the target or background even for very bright targets, demonstrating that the systematic errors are well removed. This self-referential photometry eliminates nearly all common-path systematics and allows for a theoretical differential photometric precision on the order of 10 to 25 ppm.[25]

3 Optical Design

Typically, exoplanet transmission spectroscopy is conducted using higher-resolution spectroscopic instruments ($R = \lambda/\delta\lambda$ of hundreds to thousands) on large ground and space-based observatories. These instruments are not specialized for the specific task of obtaining exoplanet transmission spectra and are, perhaps unsurprisingly, sub-optimal for the task. Specifically, there is typically substantial room for improvement in the instrument transmission and systematic errors. Data reduction processes can be greatly eased (thereby decreasing systematic errors) by building an instrument that produces isolated, binned spectral measurements rather than needing to extract, calibrate, and bin high spectral resolution data.

ETSI is a purpose-built instrument designed specifically to reduce systematic errors and produce high photometric precision exoplanet transmission spectra. The requirements considered throughout the optical design process are listed below.

1. Optimization wavelengths 430 to 975 nm: Wavelength coverage was driven by coverage of modeled exoplanet atmospheric features and constrained by the sensitivity of the ETSI detectors.
2. Compatible with $f/8$ or slower telescopes: We envisioned ETSI traveling to multiple telescopes (e.g., both Northern and Southern hemisphere telescopes), and this ensured compatibility with a variety of potential telescopes. Currently, ETSI has only been paired with the McDonald Observatory 2.1-m telescope as it has sufficient aperture for exoplanet targets, is easy to interface with, and has a sufficient number of available nights for commissioning and science observations.
3. Moderate focal reduction: The dispersed nature of the ETSI images means that each band covers a fairly large number of pixels, which would be exacerbated by use at any telescope with a large focal ratio. Focal reduction also increases the field of view to increase the likelihood of comparison stars, which may be useful during data reduction.
4. Imaging quality sufficient to ensure seeing limited performance: This also ensures that any residual color or minor focus changes affect the PSF of each filter band $\sim$ equally.
5. Maintain the angle of the multi-chroic at 30 deg or less: driven by the difficulty of designing the multiband filters at higher angles of incidence.
6. Maintain at least 20 mm of distance between the final camera optical element and the focal plane: This is a reasonable distance that was compatible with the majority of currently available detectors that were considered.

Additional considerations for each optical assembly are described in Secs. 3.1–3.3.

3.1 Collimator and Cameras

ETSI has a five-element collimator and two identical six-element cameras, as shown in Fig. 2. The optical prescription is given in Table 3 in the Appendix. The collimator is a reverse telephoto with the five lenses separated into three groups. Much of the design effort was focused on extending the distance from the last element of the collimator to the pupil. This was required to accommodate the 30-deg angle of the multi-chroic to ensure there was adequate mechanical space for the prism in the reflected channel and that the collimator and camera lens barrels would have adequate clearance as well as space for a shutter to facilitate capturing calibration frames.

The six-element cameras are split into three groups, with the final element being a field flattener. The camera optimization was constrained by the requirements listed above, as well

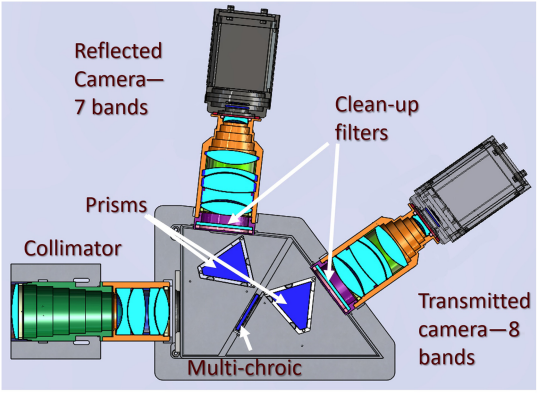

Fig. 2 Section view of the ETSI optics and detectors. The telescope focal plane is to the left of the image. Light enters the collimator and is split into two channels by the multi-chroic, which is located at the pupil. Identical prisms disperse the light, which is then further filtered to sharpen the transmission cut on/off transitions and imaged with identical cameras onto sCMOS detectors.

as the required mechanical spacing between the pupil and front lens to accommodate the prisms and clean-up filters.

All lens elements for both collimator and cameras are air-spaced with spherical surfaces. The camera and collimator were first developed separately, and then, the majority of the optimization was as a complete system to set the collimator-prism-camera angles as well as tune the prisms to achieve the desired spacing between filter bands (the simulated spacing between bands ranges between 402 and 754 μm or 36.5 to 68.5 pixels for 11-μm pixels). The band spacing was fairly conservative to account for the possibility of bad seeing and/or the potential for filter transmission/reflection transitions that were not as steep as desired. In the end, the filters that were produced were of excellent quality, and the prism dispersion could have been reduced.

Final optimization of the optical design involved extensive discussion with the optical manufacturer (JML Optical) about glass blank availability and constraints on lens sizes as well as optimization of glass choices for a minimum axial color. Of particular use was a technique where all air and glass thicknesses and surface radii were held fixed and only glass substitution was enabled for a limited catalog of glass types. The glass types were based on vendor availability, with some exclusions due to cost or manufacturing concerns. The merit function weights used in the original optical optimization were almost entirely set to zero for the glass substitution optimization. Constraints remained on the focal length and axial color, and final optimization minimized the root mean square change in focal length at each of the ETSI filter bands.[26]

Manufacturing tolerances were determined for each lens as well as positional tolerances for both individual elements and optical sub-assemblies (collimator lens barrel, prism, camera lens barrel, filters). Scratch/dig surface quality tolerance was 20-10 to ensure minimal scattered light.

In combination with the McDonald Observatory 2.1-m telescope ($f/13.7$ at Cassegrain focus), ETSI has an overall focal ratio of $f/6$, which results in a plate scale of $0.18''$/pixel and a $6.2'$ field of view. ETSI re-images a 72-mm diameter field to a 32-mm diameter image circle.

3.2 Filters

The key optical components that make ETSI possible are the multi-chroic and clean-up filters in each channel. These filters are thin film optical interference filters with many alternating layers of high and low-index dielectric materials. Filters are generally deposited using physical vapor deposition in vacuum chambers, and layers are controlled to within a few nanometers of physical thickness. A complete description of the filters and the filter design process is given in Limbach et al.[20] The multi-chroic is located at the pupil and is responsible for the initial splitting of the light into eight transmitted bands and seven reflected bands. The 30-deg angle of the multi-chroic and the out-of-band blocking (optical density 3 req. optical density 4 goal) and transmission to reflection transition zones made it difficult to meet specifications with only a single optic, so each camera has a clean-up filter to improve out-of-band blocking and cut-on/off sharpness for each of the 15 filter bands.

The filter bands were chosen to coincide with exoplanet atmospheric features. We modeled dozens of exoplanet atmospheres using Exo-Transmit[27] and aligned the spectral bands with detectable molecular and atomic absorption features.[20] Two small portions of the spectrum (680 to 697 nm and 797 to 847 nm) are blocked completely to maintain adequate spacing between spectral bands of interest on the detectors. Figure 3 shows the combined transmission of the ETSI optical components, separated into reflected and transmitted bands. The filter bands are listed in Table 2.

ETSI measures 15 simultaneous bandpasses, but in principle, two (one reflected, one transmitted) to ~50 (25 reflected, 25 transmitted) bands are possible with current technology. Larger numbers of bands require the bands to be spaced equally in wave number to maximize the filter efficiency and achieve the required cut-on/off transmission slope.

3.3 Prisms

To perform photometry on each band, prisms (N-SF5 glass type) disperse the light, separating the filter bands into distinct PSFs, which results in the unique dashed-line appearance of ETSI images (see Fig. 4).

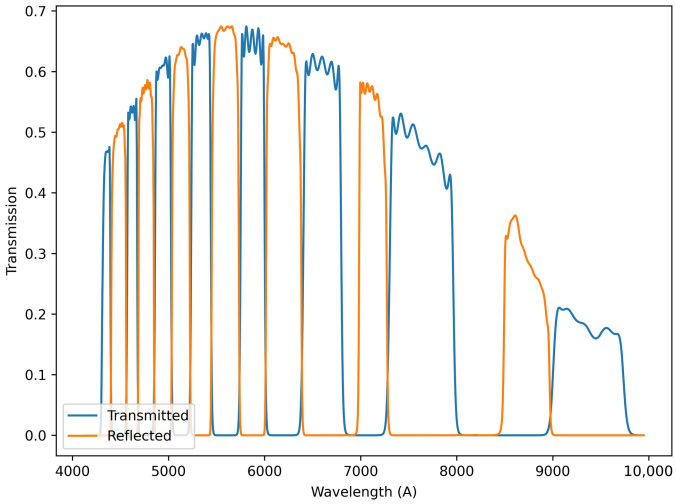

Fig. 3 Efficiency of both channels, including collimator, multi-chroic, prisms, clean-up filters, camera optics, and detector quantum efficiency from vendor measurements. The gap in coverage at ~6900 Å and ~8250 Å is to ensure sufficient separation between bands on the detector when dispersed.

Table 2 Selected ETSI filter bands.

Band	[R]eflected or [T]ransmitted	λ on $-\lambda$ off (nm)	Target feature
1	*T*	430 to 440	Rayleigh
2	*R*	440 to 456.5	Rayleigh
3	*T*	456.5 to 468	Rayleigh
4	*R*	468 to 485.5	Rayleigh
5	*T*	485.5 to 503	Rayleigh
6	*R*	503 to 523	Reference
7	*T*	523 to 544	Reference
8	*R*	544 to 574.5	Na
9	*T*	574.5 to 600.5	Na
10	*R*	600.5 to 640	Na
11	*T*	640 to 680	Reference
12	*R*	697 to 729.5	Reference
13	*T*	729.5 to 797	K
14	*R*	847 to 900	CH_4
15	*T*	900 to 975	H_2O

The optical face of each prism is 75 mm on a side with a prism angle of 46.24 deg. A complete discussion of the prism design process is described in Limbach et al.[20] Attempts were made to develop a zero-deviation prism design but were ultimately discarded due to the number of prism elements and materials required, and space constraints. The blue bands are slightly over-dispersed and produce a lower signal-to-noise ratio (SNR), especially on cooler stars. However, multiple bands in the blue portion of the spectrum can be combined in post-processing in cases in which the SNR is insufficient to provide useful exoplanet atmospheric

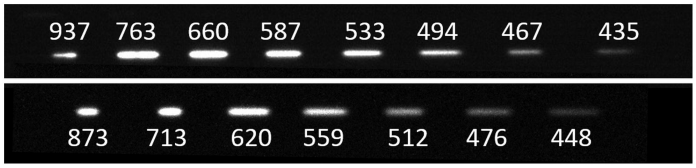

Fig. 4 Images of an F-type star showing the eight bandpasses from the transmitted channel (top) and seven bandpasses from the reflected channel (bottom), offset to show that when combined, ETSI captures almost complete wavelength coverage from 430 to 975 nm. Bands are red to blue, left to right. Central wavelength is given in nanometers above/below each band.

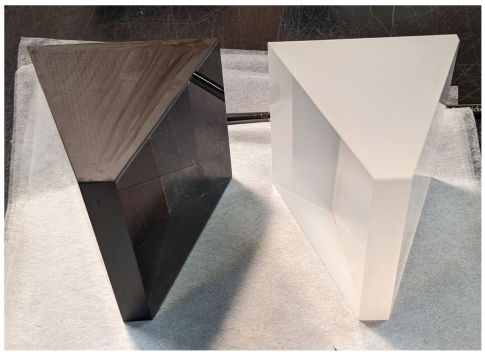

Fig. 5 ETSI prisms; the left prism has had the non-optical surfaces painted with Speedball Super Black India Ink to reduce scattered light.

constraints. Gratings were not considered due to scattered light concerns, very low required groove densities, and lower transmission when compared with prisms. Note that high instrument transmission is extremely important for exoplanet transmission spectroscopy as the exoplanet atmosphere signal is faint compared with that of the star, and sufficient photons must be collected to ensure that the planetary atmosphere signal is above the photon noise of the host star. The final prism angle and position relative to the collimator and cameras were included in the overall optical design optimization. To further minimize stray and scattered light, the non-optical surfaces of each prism were blackened with Speedball Super Black India Ink, chosen for its low reflectivity across the full optical spectrum and ease of application.[28] Figure 5 shows the dramatic difference in appearance that results from this process. After ~1 year of use, visual inspection of the blackened faces showed no apparent degradation.

4 Optomechanical Design

The optomechanical concept mimics a typical experimental setup in a laboratory, with an optical bench that all optics are mounted to with the optical axis parallel to the bench surface. The optical bench is then supported by a frame, with panels to seal the instrument from stray light and dust. Sections 4.1–4.3 describe each part in greater detail.

4.1 Commissioning Optical Bench and Support Structure

The optical bench is a lightweight, honeycomb core, composite assembly to minimize both weight and changes with temperature. Manufactured by Vere Inc., the total bench mass is 28.6 kg and is $1.0 \times 1.15 \times 0.112$ m. The top side of the bench has a grid of M6 threaded holes on a 25-mm spacing. The bottom of the bench has 3×3 equally spaced patterns of four M6 threaded holes in a square pattern, 50 mm on a side. This enables easy mounting to the support structure when mounted to the telescope, or to the top of a large laboratory optical table during alignment and testing.

The optical bench support frame was originally designed to use modular carbon fiber structural tubing, described further below. Supply chain issues and other delays required the construction of an alternate support frame (Fig. 6) from extruded aluminum structural T-slot

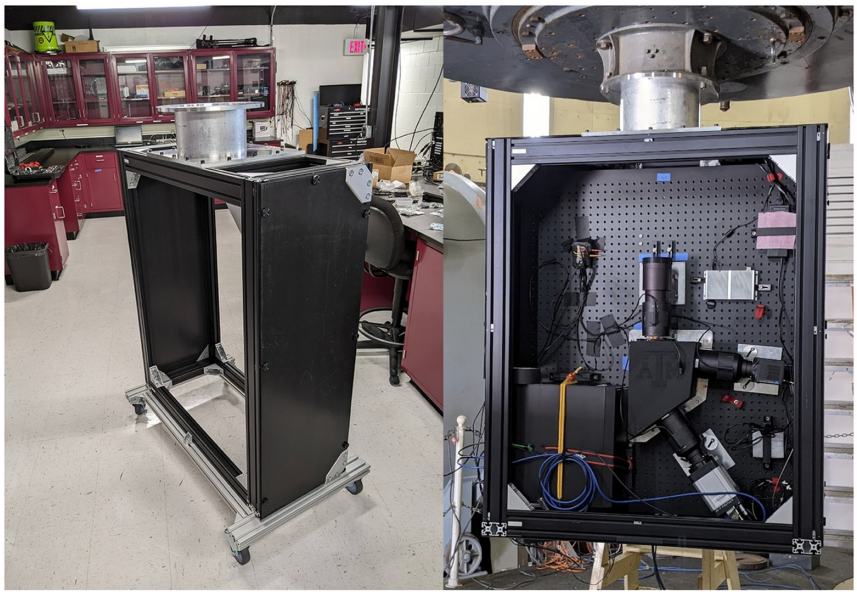

(a) (b)

Fig. 6 (a) Temporary extruded frame with two of the side panels attached; the composite optical bench has not yet been installed. A removable cart (silver extrusions) allows ETSI to be rolled around the lab or into position when mounting to the telescope. (b) ETSI mounted to the McDonald 2.1-m telescope during preparation for a commissioning run in June 2022. The front cover has been removed.

frame and fittings to finish assembly before the telescope time allocated for commissioning observations. The optical bench was rigidly supported at three points with flat aluminum plates between the bottom of the optical bench and the T-slot frame. Removable covers were constructed from corrugated plastic panels.

This support frame performed admirably during commissioning and initial science observations. Coincident with initial observations, a refined optomechanical design was developed to incorporate the originally planned carbon fiber structure while reducing the overall instrument volume. The temporary extruded aluminum enclosure was limited to targets with declination less than $+60$ deg to avoid potential collisions with the South pier of the right ascension axis of the McDonald Observatory 2.1-m telescope.

4.2 Optical Bench and Support Structure

A lightweight carbon fiber frame, constructed using a modular system from Dragonplate,[29] was designed. This system uses preformed carbon fiber tubes and gussets, which are bonded together with Scotch-Weld 2216 epoxy and held together during the curing process with pop-rivets. The tubes are easily cut to length using a standard tile-cutting wet saw to minimize carbon fiber dust. More detailed cuts were made using a rotary tool with an abrasive cutting disk while wearing a mask and a high efficiency particle arresting (HEPA) welding fume extractor placed directly above the tool, which captured the majority of the dust.

Key components are referenced in the text by letter labels in Fig. 7. The telescope-facing side of the 50-mm square tubular frame [*A*] is bonded to an interface plate made from a computer numerical control (CNC) cut sheet of 25-mm-thick structural foam core sheet material with a Divinycell H100 core[30] and three layers of plain-weave carbon fiber bonded to each side [*B*]. The carbon fiber frame and aluminum plate are bolted together and can be separated for transport. Both stainless steel bonded nuts and threaded aluminum inserts epoxied into the ends of the hollow square tubes provide six locations to bolt the two plates together [*C*]. This dual plate configuration enables a good bonding interface to the carbon fiber frame while still providing a robust aluminum interface to the telescope, which is better suited to frequent mounting to the telescope.

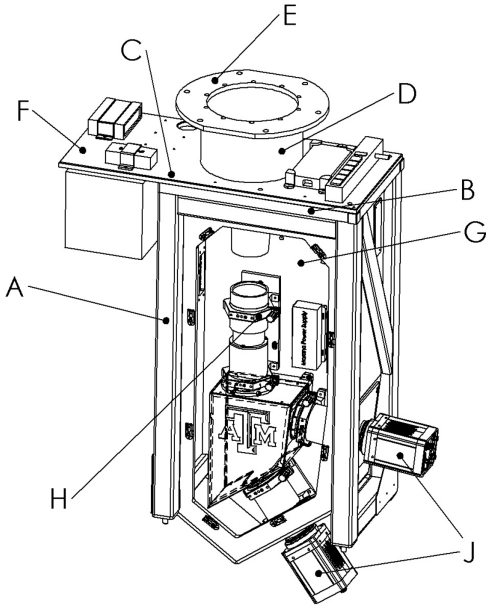

Fig. 7 Labeled components are described in detail in the text. The main access panel has been removed in this rendering to show the internal components. (a) Tubular carbon fiber frame, (b) structural foam and carbon fiber sheet interface plate, (c) bolts and threaded inserts, (d) aluminum spacer ring, (e) telescope interface ring, (f) aluminum top plate, (g) structural foam and carbon fiber optical breadboard, (h) split ring, and (j) sCMOS detector systems.

ETSI is mounted to the telescope via an aluminum spacer [D] constructed from a 152.4-mm long, 12.7-mm wall thickness tube, and 12.7-mm tool plate telescope interface ring [E] (six 1/2″-13 bolts on a 346-mm bolt circle are used to mount ETSI to the telescope). The other end of the tube bolts to the 12.7-mm-thick aluminum front plate [F].

The support structure was assembled in stages, with careful fixturing to ensure the alignment of critical pieces. Because the majority of the structural assembly is held together with Scotch-Weld 2216 epoxy, there are no second chances or repositioning once the epoxy has cured. The optical breadboard [G] is made of the same 25-mm-thick structural foam core carbon fiber sheet; it also makes up one side of the enclosure. The optics are mounted to the breadboard via stainless steel M6 bonded inserts. The holes for the inserts are cut via CNC at the same time as the overall profile of the sheet. Standard machining tolerance for the structural carbon fiber sheets is ± 0.254 and ± 0.127 mm and is possible for an additional cost. Optical tolerancing determined that the standard 0.254-mm machine tolerances were sufficient for the alignment of the collimator, filters, prisms, and cameras, and this approach was validated using the commissioning version of the support structure.

To ensure that the optical bench will locate the correct distance from the optical axis, as well as perpendicular to the telescope mounting interface, an aluminum cylinder, the same diameter as the collimator lens tube, was machined to length and mounted to the aluminum interface plate [visible in Fig. 8(a)]. A coordinate measuring arm (FARO Quantum, FARO Technologies, Inc.) was used to measure the perpendicularity, and the cylinder was shimmed with plastic shim stock to within 1 arcmin of perpendicular to the telescope interface ring. The lens assemblies are mounted via two split-ring clamps for each lens tube [H], so the collimator lens tube mount was clamped to the fixture cylinder as well as screwed to the threaded inserts bonded to the carbon fiber breadboard. The remaining degrees of freedom (rotation and translation about/along the cylinder) were set via measurement with the coordinate measuring arm, referenced to the aluminum interface plate [F] and telescope mounting flange [E]. Once in place, the split rings were tightened, and the cylinder was left in place until the structure had fully cured. The assembly continued in stages, allowing each set of pieces to cure for 24 h before additional components were bonded. The epoxy assembly steps took 3 days to complete. Figure 8 shows the alignment cylinder and partially constructed support frame as well as the completed structure mounted to the McDonald 2.1-m telescope.

(a) (b)

Fig. 8 (a) Carbon fiber support structure was built around an aluminum cylinder mounted to the aluminum interface plate and shimmed to be perpendicular to the plate. The collimator optical mount clamps to the cylinder and sets the position of the breadboard relative to the optical axis. (b) The completed carbon fiber structure mounted to the McDonald 2.1-m telescope.

The remaining side panels are made from 6.35-mm-thick structural foam core carbon fiber sheets and were also cut to size, including any necessary cut outs, via CNC. The side opposite the breadboard is mostly open and covered by a 2-mm-thick sheet of solid carbon fiber, held in place with captured hardware and sealed around the edges with 1-mm-thick adhesive-backed foam weatherstripping to prevent dust and light intrusion. All edges of the structural foam core sheet were either sealed with epoxy to other surfaces, covered with 1-mm-thick strips of carbon fiber, or for several curved and difficult-to-reach places, painted with flat black acrylic paint. Any aluminum-to-carbon fiber interfaces were separated with a thin layer of epoxy to prevent galvanic corrosion.

The two detectors $[J]$ extend outside of the enclosure, both to reduce the build-up of heat inside the enclosure, as well as provide more flexibility for using alternative detectors. The finished structure is very light weight; the complete instrument when mounted to the telescope is $\sim$70 kg, and when separated, the aluminum plate and telescope interface and carbon fiber structure (without optics, cameras, etc.) are both easily carried by a single person. The handling cart (not included in the instrument mass) is the heaviest sub-assembly.

4.3 Optical Mounts

The collimator and cameras were purchased as complete optomechanical assemblies. The design of the mounting interface between the lens barrels and supports as well as to the detectors was a cooperative effort with the vendor. The detectors are mounted with four M3 screws from the camera barrel flange to the body of the detector. The back focal spacing is set by a captured ring, machined to the correct thickness. The focus between channels is matched by placing a back-illuminated pinhole at the location of the telescope focal plane. The pinhole location is adjusted so that the transmitted camera is in focus with a spacer set for the nominal back focal distance. The reflected channel is then focused to match by adjusting the spacer between the camera barrel and detector with shims.

Each lens barrel is supported by two split rings, mounted to plates that are screwed to the optical bench threaded inserts. The front split ring for each barrel has a hole for a 3-mm pin. The lens barrels have a matching hole for the pin. The two split rings for each optical tube locate the collimator and cameras on their respective axes, whereas the pin between each tube and the first split ring sets the axial position as well as the clocking of the cameras. The lens barrels can be

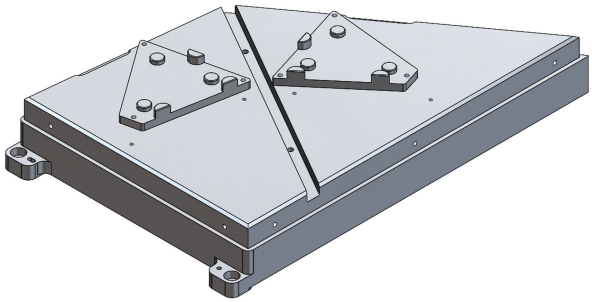

Fig. 9 Prism base. A slot for the multi-chroic mount is visible with machined prism-locating points on either side. The prism base was machined out of a single piece of 63.5-mm-thick tool plate, the underside has been light-weighted to a 5 mm wall thickness.

removed for transport to the observatory and repeatably mounted upon arrival at the telescope. ETSI has been assembled/disassembled at McDonald Observatory several times during commissioning and science observations each time the optics and cameras have been mounted to the breadboard with no additional alignment in only a few minutes. The detectors remain mounted to the lens barrels for transport.

The position of all lens barrels relative to the multi-chroic and prisms is set by the locations of the mounting screws and threaded inserts in the carbon fiber breadboard. Each optic mount uses three screws to set the location, a shoulder screw in a close-fitting hole, a shoulder screw in a close-fitting slot, and a third screw in an oversized hole. In practice, the alignment tolerances among the collimator, multi-chroic, prism, and camera barrel are loose enough that no further adjustment has been necessary after attaching all optical mounts to the breadboard. Alignment was checked using a coordinate measuring arm, and each lens barrel was within $\sim$8 arcmin of the optical axis. This level of misalignment was undetectable in lab images and negligible when modeled with Zemax. The self-referencing technique used in the ETSI instrument removes most systematic errors that would typically arise due to misalignment or flexure, thus eliminating the need for extremely tight instrument tolerances. The $f/13.7$ focal ratio of the McDonald 2.1-m telescope also eases the alignment tolerances.

The multi-chroic and prisms are mounted to an aluminum support plate that was machined out of a single piece of tool plate (Fig. 9). It has a slot to hold a plate at the 30-deg multi-chroic angle. The multi-chroic is mounted into this plate in a circular recess and held in place with a retaining ring with an o-ring spacer.

The prisms are mounted in a 3-2-1-style fixture consisting of three pads machined into the mounting plate to set the prism height and rotation along two axes, two cylindrical contact points on one face of the prism, and one cylindrical contact point on a second face. An Aluminum plate clamps the prisms onto the prism base via three long screws, one at each corner. A thin textured rubber sheet is placed between the top of the prism and the clamping plate to allow for differential expansion and contraction due to temperature changes. Baffles were 3D-printed, and internal surfaces were coated with adhesive-backed light-absorbing Fineshut SP urethane foam (see Ref. 21 for total reflectivity measurements of this material; the average reflectivity over the ETSI bandpass is <1%).

The prism and multi-chroic mount assembly are covered with a 3D-printed cover. The entire assembly can be removed from the breadboard by removing three M6 screws.

5 Electronics and Software

5.1 Detectors

The recent availability of high-quality optical complementary metal-oxide semiconductor (CMOS) sensors[31,32] [often referred to as scientific CMOS (sCMOS)] has proven crucial to the success of ETSI. An early ETSI prototype used a commercially available charge-coupled device (CCD). There were no issues with the data quality; however, even at the highest read-out speed, the observing efficiency was very low. To measure the small color changes during a transit, averaging over many measurements is required, and the overall sensitivity is driven by the total

number of photons detected. Especially for bright targets, the exposure time can be shorter than the read-out time of the CCD, resulting in many missed photons. In addition, read noise becomes an issue at all but the slowest read-out rates.

One possible solution considered was to switch to a frame transfer electron-multiplying CCD (EMCCD). Frame transfer allows for faster read rates, and the electron multiplication process can essentially eliminate read noise under certain observational conditions. However, for any pixels where the shot noise is above the readout noise, the SNR is reduced by a factor of $\sqrt{2}$ due to the stochastic nature of the electron multiplication process. This means that EMCCDs are best suited for low photon counts. The electron multiplication process also effectively reduces the possible dynamic range, so a 16-bit EMCCD has an equivalent, or even lower dynamic range than the 12-bit readout (many sCMOS sensors have a dual gain, 12-bit ADC) of an sCMOS detector for higher EMCCD gain values.

The latest generation of sCMOS devices solves essentially all of these issues, with future generations promising even better performance. Our chosen detector, the Andor Marana sCMOS camera is based around the GSENSE400BSI sensor, a back-illuminated, 11-μm pixel, 2048×2048 px array. The large pixel size and high quantum efficiency (peak QE of 95%) make for the efficient collection of photons and the readout time of $\sim$20 ms enables a minimum of observation time lost to readout. Read noise is $<2e^-$ at all frame rates. One aspect of the current generation of sensors we are still evaluating is the inclusion of a dual amplifier architecture, where each pixel is read by two amplifiers, each with a different gain. Two readout modes are available, either a "high gain" mode, in which a single amplifier is used and the output is a 12-bit image, or a "high dynamic range" mode where, on a pixel-by-pixel basis, a decision is made on which amplifier to use (if the high gain amplifier is saturated, the low gain amplifier is used). The two data streams (high and low gain) are digitized at 12 bits and are then set to a common linear scale and combined into a single 16-bit image. Due to the rapidly evolving sCMOS camera availability, our reflected camera has changed several times as we evaluate different models. Most reflected channel observations have been made with a Teledyne Kinetix sCMOS camera. The different format (6.5-micron pixels, 3200×3200 px array) has essentially the same field of view as the Marana camera on the transmitted channel. A Teledyne Kuro sCMOS camera is the current reflected channel camera (11-micron pixels, 2048×2048 px array) and uses the same GSENSE400BSI sensor as the transmitted channel Andor Marana. A recent award (From the Mt. Cuba Astronomical Foundation) has enabled the purchase of matching Teledyne COSMOS-10 sCMOS cameras, which have 10-micron pixels in a 3260×3260 px array and most importantly 16-bit digitization from a single readout. This will result in $0.164''$/px and a potential $8.9'$ field of view. However, the usable field of view will be less as the original optimization was for a smaller field of view, so a combination of image quality reduction and vignetting will limit the field to $\sim$7 arcminutes on the McDonald 2.1-m telescope. We expect to integrate the new cameras soon after they are delivered in 2025.

Currently, we are collecting any transit data in the "high-gain" 12-bit output mode. This can result in higher data rates ($\sim$10 frames per second for an 8th magnitude star on the McDonald 2.1-m telescope) to avoid saturation but was decided to be the conservative approach until a full analysis can be performed on the dual-readout 16-bit data. Over a full transit on bright targets, the overall data volume is substantial. For individual exposure times of less than a second, the data are saved as co-added images ($\sim 10-15$ frames per co-add) to reduce the required disk space while still providing sufficient time resolution.

5.2 Shutter, Temperature Monitoring, and Communication

ETSI has essentially no moving parts with the exception of a Uniblitz NS65B bi-stable optical shutter controlled with a Uniblitz VED24 shutter driver. The shutter is located between the collimator and multi-chroic to allow for the acquisition of dark and bias calibration frames and is mounted to the entrance port of the 3D-printed prism and multi-chroic mount cover. It is not used during normal observations due to the high frame rates (the rated continuous operation frequency is 1 Hz). Instrument internal and external temperatures are monitored via low-cost 1-wire DS18B20 temperature probes. All control and interface signals are via USB. Two operational modes have been used. The original control interface was a FireNEX-5000Plus USB 3.1 fiber optic extender, which has a four-port hub on the remote unit and is then connected to a local

Fig. 10 ETSI during assembly at McDonald Observatory. The red split rings holding the lens barrels are visible. The multi-chroic and prisms are mounted inside the black 3D-printed cover with the Texas A&M Logo. The black extruded aluminum frame holding ETSI can be rolled around the observing floor and is removed once ETSI is mounted. Spring-loaded casters allow for any misalignment as ETSI is lifted to the back of the telescope for mounting.

unit via duplex single-mode fiber. This allows the control computer to be located in the control room. In practice, even an armored casing fiber was not robust enough for long-term use as the control cable drapes from the back of the instrument, across the observatory floor and to the control room making consistent strain relief challenging. In the current configuration, an industrial control computer is mounted to the aluminum top plate that is the interface to the carbon fiber enclosure (instrument top left in Fig. 10). Instrument control is accomplished via remote desktop software. The only external cabling between ETSI and the observatory is 120 V power and Ethernet.

5.3 Camera Control

The sCMOS cameras are controlled by a Python program. The Andor Marana camera interfaces with the Andor software development kit (SDK) and andor3 Python interface.[33] The andor3 Python interface includes utilities that control the frame buffer and frame delivery to the rest of the program. The Teledyne Kinetix sCMOS camera interfaces with Teledyne programmable virtual camera access method (PVCAM) and python virtual camera access method (PyVCAM).[34] The Teledyne Kuro sCMOS camera interfaces with Teledyne PICam.[35] The Teledyne interfaces were edited to use similar frame buffer and frame delivery systems as the andor3 Python interface. A user interface allows observers to set up each acquisition sequence. Settings such as exposure time, co-add count, and gain (12-bit or 16-bit) are selected by the user and sent to the camera. When the camera is commanded to begin taking frames, the frame buffer waits for each new frame and delivers the frame to a callback function. The callback function saves each frame as a flexible image transport system (FITS) file with informational headers that include position, environmental, and tracking information from the McDonald Observatory 2.1-m telescope control system (TCS). The transmitted camera sends a Transistor-Transistor-Logic (TTL) trigger pulse to the reflected camera to ensure image acquisition is synchronized. Both cameras have native trigger I/O interfaces accessed via multi-pin to coax breakout cables. The breakout cables for trigger out/in are directly connected. The transmitted camera initiates the exposure sequence and the reflected camera starts its exposure on the rising edge of the transmitted camera "start exposure" TTL pulse.

5.4 Interface with McDonald Observatory 2.1-m Telescope TCS

The position and tracking information from the McDonald Observatory 2.1-m TCS is collected by connecting to the TCS network and requesting the information once every second. Between

each request, the information is stored, so it can be inserted into each frame's FITS header as each frame arrives. In addition, a frame or stack of frames is sent to the 2.1-m telescope's auto-guiding software, Guide82, every 10 s. Guide82 also reports the estimated full width at half maximum of the images and includes an automated focusing routine.

6 ETSI Data Reduction Pipeline

During commissioning, a Quick Look Pipeline (QLP)[21] was used to provide real-time analysis of target photometry concurrent with ETSI observations while users are at the telescope. Real-time estimates of the white light curve of the target star helped confirm that ETSI was functioning as expected. The QLP is no longer used for regular science observations.

The full data reduction suite for ETSI consists of three main components: image pre-processing, photometry extraction, and systematics removal. ETSI science images meant for relative color measurements are not calibrated using traditional photometric methods. We found that the sCMOS systems are remarkably stable and that standard flat fielding, bias subtraction, and dark correction were unnecessary to meet our science goals. These steps added noise to the data, and we were unable to generate a master bias and flat frames with noise values below the photon precision we hoped to achieve. Instead, images are co-added to a desired timescale (typically 1 minute) to reduce file size and increase measurement precision.

Photometry is extracted from each image typically using fixed-size aperture photometry (though both adaptive aperture photometry and PSF fitting are available). A master image is generated to locate the position of each spectral PSF. We found traditional star-finding routines failed with the ETSI PSF and did not order each spectral PSF in a convenient fashion. Instead, the initial location of a single PSF of the target star (and comparison star, if necessary) is manually selected on the master frame to provide an initial solution for the location of the star. The ETSI pipeline then automatically identifies the position of each PSF using the known dispersion of the instrument and centroids these positions to find the center of mass of each PSF within a box half the size of the elliptical apertures. The ETSI PSF is then extracted from each image (after re-centroiding for small shifts between images) using the PYTHON photometric software photutils.[36] The stellar flux is extracted using a fixed-size elliptical aperture of 40×25 pixels for the transmitted data and a fixed-size elliptical aperture of 65×30 pixels for the reflected data. The difference in aperture sizes reflects the difference in the pixel scale, which leads to more pixels per PSF on the reflected camera.

The sky background was estimated using a sky aperture of identical size to the target aperture, which was placed above and below the PSF of each bandpass, typically between 150 and 300 pixels of the target aperture. The sky apertures were moved closer to the target aperture or farther from the target aperture to avoid flux contamination from nearby stars. The fluxes in each sky aperture were summed, the two measurements were averaged, and the resulting value was subtracted from the total summed flux of the target aperture. The target flux was then converted into e^-/s using the total exposure time of the co-add (typically 60 s) and the gain of the detectors (0.61 e^-/ADU). The light curves were then converted to an instrumental magnitude with the standard equation

$$m_i = 25 - 2.5 \log_{10}(f_i). \tag{3}$$

Common-path systematics (e.g., those from airmass, cloud cover, and atmospheric color-terms) were removed from each light curve using a time-averaged "trend" light curve unique to each bandpass. The following process is completed for exoplanet targets. These trend light curves were generated by linearly combining all other available spectral bandpasses (across both cameras) with the equation

$$t_i = \sum_{j=0}^{N} (c_j \cdot m_j + b_j); \quad \text{where } i \neq j, \tag{4}$$

where t_i is the magnitude of the trend of the i'th spectral bandpasses, N is the number of bandpasses, m_j is the magnitude of the j'th bandpass, c_j is the best-fit scaling correction for the j^{th}

bandpass, and b_j is the best-fit shift for the j'th bandpass. This trend is generated using the linear regression function in the sklearn.linear_model PYTHON library.

The final normalized light curve for each bandpass was calculated by subtracting the trend light curve from the target light curve. This type of spectral band referencing is a common method to reduce systematics in transmission light curves and is a proven technique for exoplanet light curve analysis to reduce systematic noise sources.[37–41]

We found this method to vastly improve the capabilities of removing systematics from the target light curves over more traditional methods, such as comparison star referencing. In comparison star referencing, the light curve of a nearby bright star is subtracted from the light curve of a target star. Typically, this is a useful way to remove systematics because both stars were simultaneously observed through roughly the same atmosphere and appear at nearby positions on the detector. However, because the light from the two stars did not travel through exactly the same path prior to landing on the detector and because not every star in the sky has a nearby, similar magnitude companion, the comparison star method is not a fool-proof method to remove systematics.

We compared the precision achieved by both the common-path multi-band imaging (CMI) method and the comparison star method for 330 light curves observed on 22 separate nights. We found that, on average, the CMI method achieved better precision for ETSI light curves by a factor ~1.5 when the comparison star is within 1 magnitude of the target star (or brighter), and we only found the comparison star method to provide better precision for 7 out of 330 light curves. For example, we found the dispersion in the transit light curve of WASP-33 b dropped from $\sigma = 3 \times 10^{-3}$ to $\sigma = 3 \times 10^{-4}$, and most of the inherent stellar variability was removed from the transit light curve when using the CMI method as compared with the comparison star method, as shown in Fig. 11(b). The distribution of the ratio of the achieved precision of both methods for all 330 light curves is shown in Fig. 11(a).

Although this method is effective at removing non-astrophysical signals, it also removes common, non-color-dependent astrophysical signals, such as the mean transit signal (white-light transit) because this signal is common to all bandpasses. Therefore, a model of the white-light transit signal was injected into each bandpass's de-trended light curve prior to measuring the transit depth at each wavelength.

We found that injecting the white-light curve transit was useful for two reasons. First, we found that transit fitting routines were more capable of measuring realistic depths after a model transit was injected than they were at measuring residuals. This was particularly important

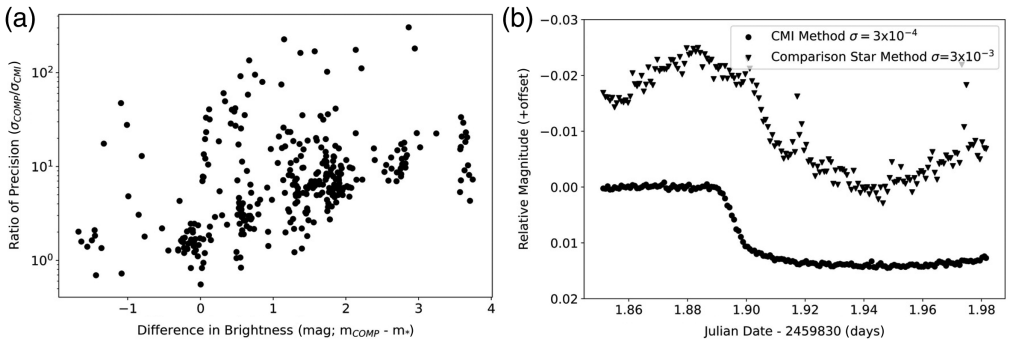

Fig. 11 (a) Comparison of the difference in brightness between the target star and comparison star and the ratio of the out-of-transit precision measured for 330 light curves observed on 22 separate nights using both the comparison star method (σ_{COMP}) and the CMI method (σ_{CMI}). On average, we find that the CMI method improves light curve precision by a factor of ~1.5 for comparison stars within 1 magnitude of the target star or brighter. We only found the comparison star method to improve the precision on 7 out of 330 light curves. (b) The achieved dispersion in the light curve of WASP-33 b observed on September 8, 2022, when using the CMI method (circles; $\sigma = 3 \times 10^{-4}$) and when using a traditional comparison star method (triangles; $\sigma = 3 \times 10^{-3}$). We find a factor of 10 improvement in out-of-transit precision quality when using the CMI method for this light curve.

for residuals containing a "negative" transit depth because the transit was shallower than the white-light signal. Second, because we injected the same white-light transit signal into each bandpass, we knew the ground truth mean transit depth "a priori." This allowed for a much more convenient comparison of the recovered signal to a flat line, which could indicate a null detection.

Next, the precision of the ETSI instrument was investigated using the light curves of the A0 star HD 9711 ($V = 9.98$)[42] to identify the minimum level of detectable color change ETSI could achieve over 3 h of observation, a similar timescale to an exoplanet transit. A-type stars are expected to have little-to-no changes in their color, and by investigating the dispersion of ETSI color curves for HD 9711, a limit can be placed on the minimum detectable color change. The change in color for each bandpass was found to be consistent with a zero-slope line in all cases (the coefficient of determination, R^2 was ~0). The standard error on the mean (binned in an interval of 200 min) was found to be 0.006%, as shown in Fig. 12. This color change is consistent with the systematic error achieved by the Hubble Space Telescope (HST) of ~0.001% to 0.01% on similar timescales.[43] This means ETSI can provide HST-quality precision for the measurement of color changes over the timescale of an exoplanet transit.

Finally, we expect future iterations of the pipeline to have the capability to substitute its self-referential photometry functions with more traditional methods to remove detector systematics from the ETSI photometry. These methods could include:

- Comparison star detrending: Typically, two stars of similar magnitude should not vary in identical astrophysical patterns between images, even if they were the same spectral type or variable type. In many cases, the bandpass-specific flux from a comparison star can be binned using a moving mean and used to normalize the target star's bandpass flux and remove common systematics.[44–46]
- Observational bias detrending: Ground-based observations will suffer from changes due to airmass, extinction from clouds, changes in the temperature of the detector, and slight changes in the position of the star on the detector. A trend could be generated through a linear or polynomial combination of these factors to remove systematics, which are not found to be correlated between the target star and its comparison.

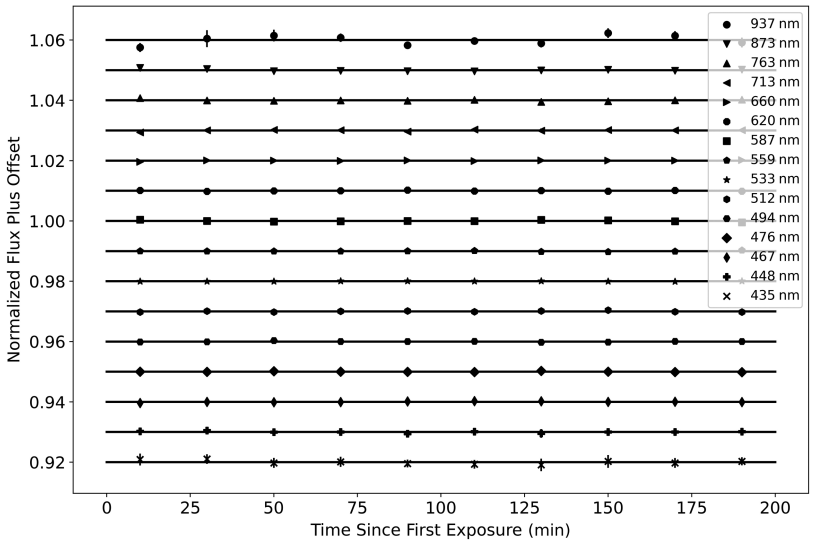

Fig. 12 Light curves for the 15 ETSI bandpasses for the A0 star HD 9711 over the course of ~200 min. Each bandpass has been cleaned using a linear combination of the other 14 bandpasses. The data have been binned into 20-min intervals and offset by 1% for clarity. The solid lines are not fit to the data, but are simply a line with zero slope at each offset. The error bars are plotted on the figure and are roughly the size of each data point or smaller. The standard error of the mean of these light curves suggests that, on average, the observations could have identified a color change of 0.006%.

7 Science with the ETSI Instrument

ETSI was primarily designed to carry out exoplanet characterization and vetting via spectral transmission measurements at $R = \lambda/\delta\lambda \approx 20$. Below, we describe this and the other potential scientific capabilities of ETSI in more detail.

ETSI characterizes exoplanet atmospheres by producing spectra in the visible ($430 < \lambda < 975$ nm) in 15 spectral bands. This is comparable to the spectral resolutions reported by other transmission spectroscopy measurements, which are typically collected at higher resolutions but binned down to increase the SNR and study the same spectral features and similar bandpasses as ETSI[47,48] or only focus on a very narrow spectral range at high resolution.[49,50] The location of the ETSI spectral band filters is designed to coincide with spectral features of interest in exoplanet atmospheres. Specifically, ETSI transmission spectra measurements are sensitive to the presence of atoms (potassium and sodium), molecules (methane, water, and TiO), and clouds and aerosols in the exoplanet's atmosphere (Rayleigh scattering). ETSI bandpasses were specifically tuned for the characterization of transiting gas-giant planets, but additional filters could be produced to match other targets.

These self-referenced differential measurements serve as a proxy for the measured atomic and molecular features in the exoplanet's atmosphere. These features can be modeled, and the atmospheric composition of the planetary atmosphere can be inferred. Spectral band referencing is used to reduce systematics in the transmission light curves and is a proven technique for exoplanet light curve analysis to reduce systematic noise sources.[39,41] Residual systematics can be removed with typical detrending techniques (i.e., polynomial detrending or Gaussian process regression[37,38,40]) in combination with time-averaged light curves from reference stars in the field of view. The best-fit exoplanet atmospheric model can then be found by using standard exoplanet atmospheric retrieval tool kits, specifically the open source python code petitRADTRANS[51,52] in combination with the emcee Markov Chain Monte Carlo framework.[53] The results of the first sample of exoplanet transits observed with ETSI are reported by Oelkers.[54]

Transits rarely required a complete night for observation, and a significant number of night time hours were available for other observations while waiting for the transit observation window. This time was used to explore other, non-transit observations that could take advantage of the simultaneous multi-band capabilities of ETSI.

Observations of existing spectrophotometric standard stars with ETSI can be used to expand the number and sky coverage of spectrophotometric standard stars. The common path and simultaneous nature of ETSI observations reduces the influence of many common photometric errors and dramatically improves the observing efficiency as there is no observing time lost to filter changes or re-observation due to weather changes half way through a filter sequence. An example is shown in Fig. 13.

ETSI also excels at observing a wide variety of variable sources. Simultaneous measurement of 15 filter bands combined with the low-read-noise, high-cadence imaging modes enabled by sCMOS detectors can be used to monitor sources that are variable on a wide range of timescales.

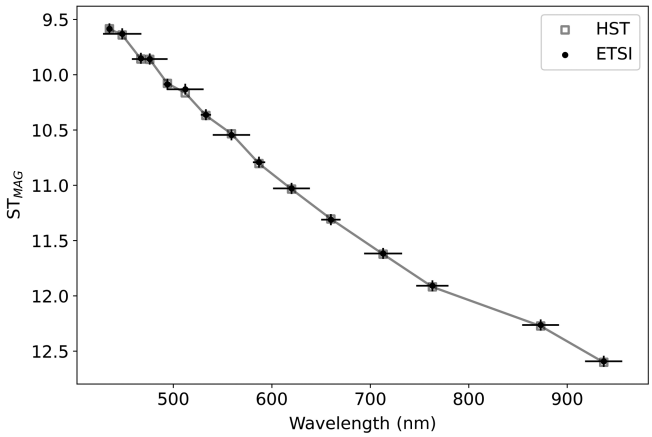

Fig. 13 Comparison of ETSI spectrophotometric measurements with an HST standard star.

Our highest cadence observations to date are 10 frames per second, sustained for 3 to 6 h. This cadence was required to avoid detector saturation, so the data were typically saved as co-added 1.5-s equivalent exposures to reduce data storage requirements, but that is not required if the higher time resolution is desired. We have observed sources that are variable on a variety of timescales, including white dwarfs (minutes), exoplanet transits, RR Lyrae (hours-days), and several supernovae (days-weeks). Representative observations of a variety of targets are shown in Sec. 8.1.

8 Commissioning

ETSI achieved first light on April 19–24, 2022, on the McDonald Observatory 2.1-m telescope with only the transmitted channel, allowing simultaneous photometry of eight spectral bands. Observations with both transmitted and reflected channels (15 bands) began on June 6–21, 2022, and the final carbon fiber support structure was first used on April 10–14, 2023, all on the McDonald Observatory 2.1-m telescope.

8.1 Preliminary Results

Light curves have been investigated for several exoplanets both during and after instrument commissioning. An in-depth discussion of these observations is forthcoming in Oelkers.[54] One such object was HAT-P-12 b (HAT-P-12, $V = 12.84$[55]), which was targeted because it has been observed with multiple other observatories and instruments, including the HST,[43] and can provide a comparison with previous results. A single partial (82% of the transit duration) transit was observed with ETSI during an observing run in June 2022 (details of the observation and analysis are in Oelkers[54]). The transit depths measured using ETSI in combination with a 2-m class telescope (that costs ~160 USD/night) were then modeled and statistically compared with the transit depths measured using HST (that costs ~100,000 USD/hour)[43] using a two-sample Anderson–Darling test. The p-value of the test was found to be $p = 0.86$, indicating that the measurements from HST and ETSI are consistent for both targets (See Fig. 14). The achieved precision of ETSI, lack of shown color change in an A0 star, and the recovery of consistent transit depths between ETSI and HST provide substantial proof of concept evidence that an atmospheric detection can be made using a 2-m class ground-based telescope and ETSI.

Exoplanet atmosphere characterization using ETSI could be leveraged to prioritize the most interesting targets for follow-up observations using JWST. Over-subscription rates for JWST are increasing (7.3× for cycle 2,[56] 9× in cycle 3[57]), so any pre-filtering of potential targets that can occur will be a benefit to the overall community.

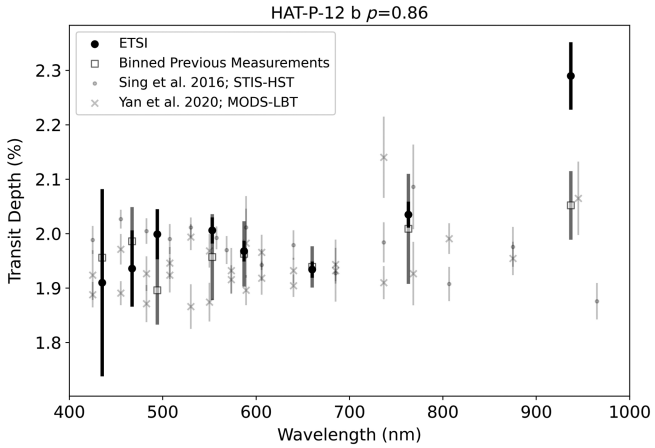

Fig. 14 Comparison of the measured transit depths for HAT-P-12b using data measured with HST [43, grey circles (original data)], LBT [64, grey crosses (original data)], and ETSI (black dots). The grey square represents the HST and LBT data binned to match the ETSI bandpasses. The uncertainties in the bins represent the scatter in the original data's spectrum at the given instrument wavelengths. The measurements are consistent within the uncertainties and an Anderson–Darling test returned a p-value of $p = 0.86$, suggesting the measurements from HST, LBT, and the ETSI instrument are consistent.

Several spectrophotometric standard stars were observed with ETSI to estimate the level of precision it could achieve for flux calibration in the following manner. First, we zeropointed ETSI observations of the standard star HZ44 to the CALSPEC library of composite stellar spectra from HST.[58–61] We then applied these zeropoints to the ETSI observations of the standard star BD +28-4211 and compared our calibrated flux measurements to the CALSPEC composite stellar spectra of the star. As shown in Fig. 13, ETSI produces excellent spectrophotometric calibration across all 15 filter bands (within 0.9%) for stars with brightness $5 < V < 14$ magnitudes with <1 h of observations.

Exoplanet transit measurements look for color changes on hours-long timescales. ETSI also excels at measuring color variability at much shorter time intervals. The white light variability of the white dwarf GD358 has been previously measured.[62] ETSI observations reveal possible color variability on similar timescales (5 s reported in the literature[62] and 20 s measured with ETSI). Normalized flux and normalized color plots of GD358 are shown in Fig. 15.

As demonstrated by the observations of HZ44 and BD+28-4211, ETSI observations can reach 1% spectrophotometric precision across 15 filter bands with only a short (<1 h) observation time. Sensitivity to color changes, as demonstrated by the observations of the A0 star HD 9711, makes ETSI a useful tool to rapidly categorize the type and redshift of bright supernovae. We are exploring the brightness and precision limits of these measurements as well as developing additional data reduction techniques to deal with the complicated background introduced by the host galaxy and other nearby galaxies. We currently use the same multi-band filter that was optimized for exoplanet transit spectroscopy, but we are exploring other bandpass combinations that are better suited to supernova characterization. An example frame from an observation of SN 2022 h is shown in Fig. 16. Expected alert rates from LSST are ~200 SNe alerts per visit.[63] Rapid follow-up observations with other telescopes will be critical to extracting useful information from these alerts.

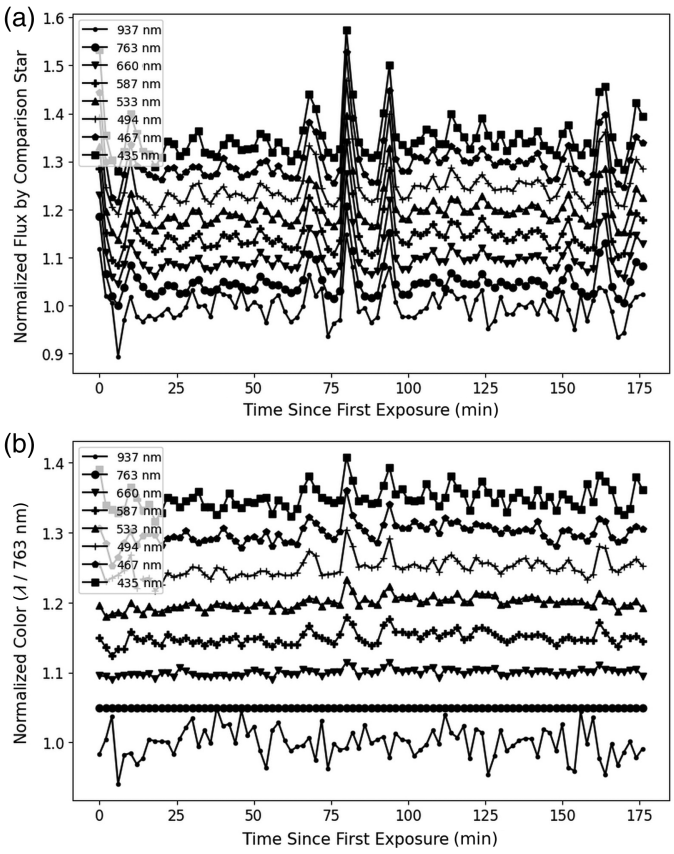

Fig. 15 Light curve (a) and simultaneously measured optical colors (b) for the ~13.6 magnitude pulsating white dwarf GD358. Note easily detected ~0.05 magnitude bluer color of the ~30% brightness increases at around 80 and 90 min. Data were offset by 0.05 magnitude for clarity.

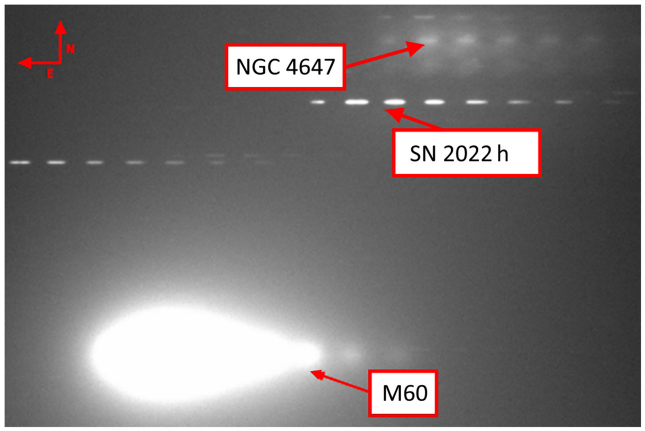

Fig. 16 ETSI multi-band image of SN 2022 h. We have achieved <1% photometric precision in measuring supernova despite the complicated background from nearby galaxies. The multi-band nature of ETSI images could enable both supernova type and redshift identification using a single ETSI exposure.

9 Conclusions

ETSI is a unique instrument that leverages the advantages of simultaneous multi-band photometry and is made possible by several key technologies, including multi-band interference filters and sCMOS detectors. Early results are promising and indicate that ETSI will be a highly productive instrument, characterizing exoplanet atmospheres in only a few transits and may be useful for JWST target prioritization and rapid follow-up of LSST transient alerts. We are actively exploring ETSI's applicability to other science targets such as supernovae, variable stars, and rapid characterization of other transient events. ETSI has observed more than 90 nights between June 2022 and June 2024 and has obtained transmission spectra of 21 exoplanets[54] during these observations as well as observations of white dwarfs, brown dwarfs, standard stars, planetary nebulae, a stellar occultation of Titan, supernovae, and blazars. Work is ongoing to refine data reduction techniques for the unique multi-band images generated by ETSI.

10 Appendix A: Optical Prescription

The ETSI optical layout is shown in Fig. 17 and the prescription in Table 3.

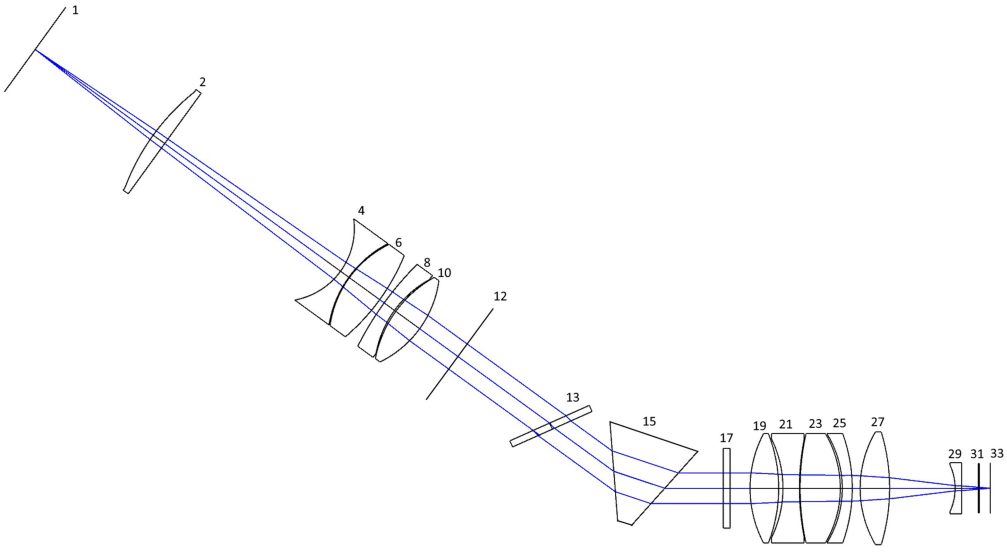

Fig. 17 ETSI optical layout, showing only the transmitted channel. Each element is identified by the number of their first surface in Table 3. The reflected channel is identical, only with surface 13 replaced by a reflection from the first surface of the multi-chroic.

Table 3 ETSI optical prescription. Radius, thickness, and diameter are in millimeters. The reflected channel is identical, only with surface 13 replaced by a reflection from the first surface of the multi-chroic.

Surface	Radius	Thickness	Glass	Diameter	Comment
1	Infinity	108.986	—	72.0	Telescope focal plane
2	165.729	10.628	S-BAL35	92.8	Collimator L1
3	Infinity	162.346	—	92.8	—
4	−54.179	7.670	N-KZFS2	67.5	Collimator L2
5	83.360	0.497	—	67.5	—
6	79.519	28.000	S-BAL3	73.3	Collimator L3
7	−158.561	4.130	—	73.3	—
8	237.390	9.491	S-BSM15	75.5	Collimator L4
9	78.961	1.250	—	75.5	—
10	88.455	22.002	S-FPL55	75.5	Collimator L5
11	−79.436	15.000	—	75.5	—
12	Infinity	105.000	—	30.3	Shutter
13	Infinity	5.000	N-BK7	65.0	Multichroic—30-deg tilt
14	Infinity	60.000	—	65.0	—
15	Infinity	40.000	N-SF5	75.0	Prism
16	Infinity	45.000	—	75.0	—
17	Infinity	5.000	N-BK7	88.5	Clean-up filter
18	Infinity	15.000	—	88.5	—
19	87.696	21.358	S-FPL51	81.6	Camera L1
20	−112.607	3.219	—	81.6	—
21	−83.695	12.324	S-LAL13	81.6	Camera L2
22	191.915	0.530	—	81.6	—
23	193.382	30.000	S-FPL51	85.5	Camera L3
24	−80.456	1.478	—	85.5	—
25	−78.202	7.431	S-LAL13	76.9	Camera L4
26	−119.932	5.911	—	76.9	—
27	83.321	22.000	S-FPL55	84.1	Camera L5
28	−144.369	48.949	—	84.1	—
29	−41.501	4.999	S-LAH63	38.2	Camera L6
30	Infinity	15.000	—	38.2	—
31	Infinity	2.500	NIFS-V	45.6	Detector window
32	Infinity	4.300	—	45.6	—
33	Infinity	—	—	32.0	Image plane

Disclosures

The authors have no conflicts of interest to declare.

Code and Data Availability

The data that support the findings of this article are not publicly available as they are included only to demonstrate the range of scientific capabilities of ETSI. They can be requested from the author at lschmidt@yerkesobservatory.org

Acknowledgments

Texas A&M University thanks Charles R. '62 and Judith G. Munnerlyn, George P. '40 and Cynthia Woods Mitchell, and their families for support of astronomical instrumentation activities in the Department of Physics and Astronomy. The ETSI project is funded by the NSF MRI (Grant No. 1920312) and the Mt. Cuba Astronomical Foundation. The authors would like to thank John Kuehne for his assistance with integrating ETSI control software with the 2.1-m TCS and Coyne Gibson for his support in developing the mechanical interface between ETSI and the 2.1-m telescope.[64]

References

1. T. Walraven and J. H. Walraven, "A new photoelectric method of classification of luminosity and spectral type for O and B type stars," *Bull. Astron. Inst. Netherlands* **15**, 67–83 (1960).
2. R. Florentin Nielsen, P. Nørregaard, and E. H. Olsen, "First fully automatic telescope on La Silla," *Messenger* **50**, 45–46 (1987).
3. S. Falter et al., "Simultaneous time-series spectroscopy and multi-band photometry of the sdBV PG1605 +072*," *Astron. Astrophys.* **401**(1), 289–296 (2003).
4. S. Ciceri et al., "Physical properties of the planetary systems WASP-45 and WASP-46 from simultaneous multiband photometry," *Mon. Not. R. Astron. Soc.* **456**, 990–1002 (2015).
5. Y.-P. Yang et al., "Multiband simultaneous photometry of Type II SN 2023ixf with Mephisto and the twin 50-cm telescopes," arXiv:2405.08327 (2024).
6. M. Mori et al., "Characterization of starspots on a young M-dwarf K2-25: multiband observations of stellar photometric variability and planetary transits," *Mon. Not. R. Astron. Soc.* **530**, 167–189 (2024).
7. M. E. Everett and S. B. Howell, "A technique for ultrahigh-precision CCD photometry," *Publ. Astron. Soc. Pac.* **113**, 1428–1435 (2001).
8. Ž. Ivezić et al., "Sloan digital sky survey standard star catalog for stripe 82: the dawn of industrial 1% optical photometry," *Astron. J.* **134**, 973–998 (2007).
9. T. Li et al., "Monitoring the atmospheric throughput at Cerro Tololo Inter-American Observatory with aTmCam," *Proc. SPIE* **9147**, 91476Z (2014).
10. D. Mislis et al., "High-precision multiband time series photometry of exoplanets Qatar-1b and TrES-5b," *Mon. Not. R. Astron. Soc.* **448**, 2617–2623 (2015).
11. N. Narita et al., "MuSCAT2: four-color simultaneous camera for the 1.52-m Telescopio Carlos Sánchez," *J. Astron. Telesc. Instrum. Syst.* **5**(1), 015001 (2018).
12. M. W. McElwain et al., "NIMBUS: the near-infrared multi-band ultraprecise spectroimager for SOFIA," *Proc. SPIE* **8446**, 84467B (2012).
13. J. M. Christille et al., "SIOUX project: a simultaneous multiband camera for exoplanet atmospheres studies," *Proc. SPIE* **9908**, 990857 (2016).
14. V. S. Dhillon et al., "ULTRACAM: an ultrafast, triple-beam CCD camera for high-speed astrophysics," *Mon. Not. R. Astron. Soc.* **378**, 825–840 (2007).
15. B. Stalder et al., "PISCO: the parallel imager for southern cosmology observations," *Proc. SPIE* **9147**, 91473Y (2014).
16. M. Robberto et al., "SCORPIO: the Gemini facility instrument for LSST follow-up," *Proc. SPIE* **10702**, 107020I (2018).
17. A. Johansen et al., "Multiband coated filters redefine performance standards for scientific applications," *Laser Focus World*, 50–53 (2016).
18. J. P. Gardner et al., "The James Webb Space Telescope," *Space Sci. Rev.* **123**, 485–606 (2006).
19. Ž. Ivezić et al., "LSST: from science drivers to reference design and anticipated data products," *Astrophys. J.* **873**, 111 (2019).
20. M. A. Limbach et al., "The Exoplanet Transmission Spectroscopy Imager (ETSI)," *Proc. SPIE* **11447**, 114477D (2020).
21. L. M. Schmidt et al., "The Exoplanet Transmission Spectroscopy Imager (ETSI), a new instrument for rapid characterization of exoplanet atmospheres," *Proc. SPIE* **12184**, 1218486 (2022).

22. L. Kreidberg et al., "Clouds in the atmosphere of the super-Earth exoplanet GJ1214b," *Nature* **505**, 69–72 (2014).
23. N. H. Allen et al., "HST SHEL: enabling comparative exoplanetology with HST/STIS," arXiv:2405.20361 (2024).
24. L. V. Mugnai et al., "Comparing transit spectroscopy pipelines at the catalogue level: evidence for systematic differences," *Mon. Not. R. Astron. Soc.* **531**, 35–51 (2024).
25. M. A. Limbach et al., "Common-path multiband imaging (CMI): a new technique for measuring precision photometric colors," (in prep.).
26. R. Siew, "Practical automated glass selection and the design of apochromats with large field of view," *Appl. Opt.* **55**, 9232–9236 (2016).
27. E. M. R. Kempton et al., "Exo-transmit: an open-source code for calculating transmission spectra for exoplanet atmospheres of varied composition," *Publ. Astron. Soc. Pac.* **129**, 044402 (2017).
28. L. M. Schmidt et al., "Characterization of the reflectivity of various black and white materials," *Proc. SPIE* **11451**, 114512S (2020).
29. Allred & Associates, Inc., "DragonPlate engineered carbon fiber composites," https://dragonplate.com/ (2024).
30. Diab Group, "Divinycell H100," (2024), https://diab-media.azureedge.net/eyajkrhd/diab-divinycell-h-october-2023-rev23-si.pdf.
31. Andor, "sCMOS camera series," https://andor.oxinst.com/products/scmos-camera-series/ (2024).
32. Teledyne, "Scientific imaging," https://www.teledyneimaging.com/en/scientific/ (2024).
33. P. Tapping, "andor3," https://andor3.readthedocs.io/en/latest/ (2021).
34. T. Hanak, "Pyvcam," https://github.com/photometrics/pyvcam (2024).
35. T. Liakat, "Picam," https://github.com/sliakat/spereadpy/blob/main/picampy/linux/picam.py (2024).
36. L. Bradley et al., "astropy/photutils: 1.0.0," (2020).
37. K. M. S. Cartier et al., "Near-infrared emission spectrum of WASP-103b using Hubble Space Telescope/wide field camera 3," *Astron. J.* **153**, 34 (2017).
38. T. Louden et al., "A precise optical transmission spectrum of the inflated exoplanet WASP-52b," *Mon. Not. R. Astron. Soc.* **470**, 742–754 (2017).
39. K. B. Stevenson, "A new method for studying exoplanet atmospheres using planetary infrared excess," *Astrophys. J.* **898**, L35 (2020).
40. J. Kirk et al., "ACCESS and LRG-BEASTS: a precise new optical transmission spectrum of the Ultrahot Jupiter WASP-103b," *Astron. J.* **162**, 34 (2021).
41. E. Ahrer et al., "LRG-beasts: sodium absorption and Rayleigh scattering in the atmosphere of WASP-94ab using NTT/EFOSC2," *Mon. Not. R. Astron. Soc.* **510**, 4857–4871 (2022).
42. E. Høg et al., "The Tycho-2 catalogue of the 2.5 million brightest stars," *Astron. Astrophys.* **355**, L27–L30 (2000).
43. D. K. Sing et al., "A continuum from clear to cloudy hot-Jupiter exoplanets without primordial water depletion," *Nature* **529**, 59–62 (2016).
44. L. Wang et al., "Photometry of variable stars from dome A, Antarctica: results from the 2010 observing season," *Astron. J.* **146**, 139 (2013).
45. A. Vanderburg and J. A. Johnson, "A technique for extracting highly precise photometry for the two-wheeled Kepler mission," *Publ. Astron. Soc. Pac.* **126**, 948 (2014).
46. R. J. Oelkers and K. G. Stassun, "Precision light curves from TESS full-frame images: a difference imaging approach," *Astron. J.* **156**, 132 (2018).
47. F. Pont et al., "Detection of atmospheric haze on an extrasolar planet: the 0.55–1.05 μm transmission spectrum of HD 189733b with the HubbleSpaceTelescope," *Mon. Not. R. Astron. Soc.* **385**, 109–118 (2008).
48. L. Kreidberg et al., "A detection of water in the transmission spectrum of the hot Jupiter WASP-12b and implications for its atmospheric composition," *Astrophys. J.* **814**, 66 (2015).
49. A. Wyttenbach et al., "Spectrally resolved detection of sodium in the atmosphere of HD 189733b with the HARPS spectrograph," *Astron. Astrophys.* **577**, A62 (2015).
50. N. P. Gibson et al., "Detection of Fe I in the atmosphere of the ultra-hot Jupiter WASP-121b, and a new likelihood-based approach for Doppler-resolved spectroscopy," *Mon. Not. R. Astron. Soc.* **493**, 2215–2228 (2020).
51. P. Mollière et al., "petitRADTRANS. a Python radiative transfer package for exoplanet characterization and retrieval," *Astron. Astrophys.* **627**, A67 (2019).
52. P. Mollière et al., "Retrieving scattering clouds and disequilibrium chemistry in the atmosphere of HR 8799e," *Astron. Astrophys.* **640**, A131 (2020).
53. D. Foreman-Mackey et al., "emcee: The MCMC hammer," *Publ. Astron. Soc. Pac.* **125**, 306–312 (2013).
54. E. A. Oelkers, "Ground-based reconnaissance observations of 21 exoplanet atmospheres with the exoplanet transmission spectroscopy imager," in prep (2024).
55. J. D. Hartman et al., "HAT-P-12b: a low-density sub-Saturn mass planet transiting a metal-poor K Dwarf," *Astrophys. J.* **706**, 785–796 (2009).

56. Space Telescope Science Institute, "General observer programs in cycle 2," https://www.stsci.edu/jwst/science-execution/approved-programs/general-observers/cycle-2-go (2023).
57. Space Telescope Science Institute, "General observer programs in cycle 3," https://www.stsci.edu/contents/news/jwst/2023/jwst-observers-set-world-record-for-astronomical-proposal-submissions (2023).
58. J. B. Oke, "Faint spectrophotometric standard stars," *Astron. J.* **99**, 1621 (1990).
59. Space Telescope Science Institute. "CALSPEC," (2023, April). https://www.stsci.edu/hst/instrumentation/reference-data-for-calibration-and-tools/astronomical-catalogs/calspec (accessed 30 May 2024).
60. R. C. Bohlin, I. Hubeny, and T. Rauch, "New grids of pure-hydrogen white Dwarf NLTE model atmospheres and the HST/STIS flux calibration," *Astron. J.* **160**, 21 (2020).
61. R. C. Bohlin and S. Lockwood, "Update of the STIS CTE correction formula for stellar spectra," Instrum. Sci. Rep. ACS 2022-5, 11 pages (2022).
62. D. E. Winget et al., "Photometric observations of GD 358: OB white dwarfs do pulsate," *Astrophys. J. Lett.* **262**, L11–L15 (1982).
63. M. Graham et al., "DMTN-102, LSST alerts: key numbers," tech. rep., Vera C. Rubin Observatory (2024).
64. F. Yan et al., "LBT transmission spectroscopy of HAT-P-12b. Confirmation of a cloudy atmosphere with no significant alkali features," *Astron. Astrophys.* **642**, A98 (2020).

Luke M. Schmidt is the Yerkes Observatory Project Scientist and was previously an associate research scientist at Texas A&M University in the Department of Physics and Astronomy (2015–2024) and an instrument scientist at the Magdalena Ridge Observatory Interferometer (2013–2015). He received his BS degree in physics and chemistry from Bethel College, KS in 2003, his MS degree in physics from the New Mexico Institute of Mining and Technology in 2009, and his PhD in physics with a dissertation in astrophysics from the New Mexico Institute of Mining and Technology in 2012. His research focuses on astronomical instrumentation in the optical and near infrared and includes instruments for imaging, spectroscopy, interferometry, and telescope calibration systems. He is a member of SPIE.

Biographies of the other authors are not available.